



Unique two-electron transfer pathway of Bismuth nanocrystal for enhanced N₂ electroreduction revealed by *in situ* infrared spectroscopy

Xin Li^{a,b}, Guangtong Hai^a, Gaofeng Chen^c, Jin Liu^b, Fenglin Zhao^a, Jinsong Zhou^b, Michael K. H. Leung^{b,*}, Haihui Wang^{a,*}

^a Beijing Key Laboratory of Membrane Materials and Engineering, Department of Chemical Engineering, Tsinghua University, Beijing 100084, PR China

^b Ability R&D Energy Research Centre, School of Energy and Environment, City University of Hong Kong, 999077, the Hong Kong Special Administrative Region of China

^c Department of Colloid Chemistry, Max-Planck Institute of Colloids and Interfaces, Research Campus Golm, Am Mühlenberg 1, 14476 Potsdam, Germany

ARTICLE INFO

Keywords:

Nitrogen electroreduction
Two-electron transfer pathway
Reaction mechanism
Bi particle sizes
In situ monitoring

ABSTRACT

Due to the alarming increase in anthropogenic greenhouse gas emissions, there is an urgent need to replace the fossil fuel-driven Haber-Bosch process with green ammonia production. Electrochemical nitrogen fixation has shown preliminary promise for industrially ammonia synthesis, but an in-depth mechanistic understanding of the nitrogen reduction process remains limited. Herein, a unique dinitrogen desorption mechanism for the nitrogen reduction reaction is detected on the bismuth nanocrystals, which may explain some intriguing phenomena reported in previous works, including (1) why hydrazine is still generated in some nitrogen reduction reactions that do not follow the alternating pathway, and (2) a minor change in bismuth particle size can lead to a dramatic change in NRR performance. In addition, the experimental and theoretical calculation results reveal that the dinitrogen desorption pathway involving the transfer of two electrons usually shows lower energy barriers and faster reaction kinetics, resulting in a dramatic enhancement in NRR performance.

1. Introduction

Ammonia (NH₃) is a molecule gaining extensive interest as an important, sustainable fuel for global use in the future. Applications of NH₃ in agriculture, heavy transport, power generation, and distributed energy storage are being actively developed [1,2]. The synthesis of NH₃ from molecular nitrogen and hydrogen using the Haber-Bosch (HB) process was one of the greatest inventions of the 20th century, and it remains the source of most of the world's NH₃ today, accounting for 90% of annual production [3,4]. However, the fossil-fuel-based HB process emits an enormous amount of greenhouse gases (GHG), with a global average of 2.9 tons of carbon dioxide (CO₂) per ton NH₃. This process is responsible for nearly 1.0% of global GHG emissions. In 2021, the total global production of ammonia reached 150 million metric tons per year, and the demand is expected to reach 350 million metric tons per year by 2050. Therefore, it is urgent to search for sustainable, cost-effective, and zero-carbon emission methods for NH₃ synthesis [5–9]. In this vein, nitrogen fixation through electrochemical nitrogen reduction reaction (NRR) has been identified as a logical approach as solar photovoltaic or wind-power electricity can directly drive the NRR

activities [10–13]. However, most reports concerning this reaction still exhibit production rates less than 1 nmol s^{−1} cm^{−2} [14–19], which is at least two orders of magnitude below the industrial target for this process [20–26].

Deep insights into the catalytic process to explore the reaction mechanism of NH₃ synthesis would provide guidelines for developing more advanced catalysts to improve the production rate [27–30]. So far, there are four generally accepted mechanisms for N₂ reduction, namely, dissociative, associative (including distal, alternating and enzymatic), Mars–Van Krevelen and surface hydrogenation mechanisms [31,32]. For all these mechanisms, the entire conversion process of N₂ to NH₃ molecules occurs on the catalyst surface, and thus a six-electron transfer process is an essential prerequisite to efficiently catalyze NRR [33–35]. However, some intriguing phenomena in the previously reported experimental works are difficult to explain by the mechanisms mentioned above. For instance, the by-product hydrazine (N₂H₄) is often generated if the two nitrogen atoms are protonated alternatively. However, some experimental works reported that a certain amount of N₂H₄ could still be detected when catalysts did not follow the alternating pathway to synthesize NH₃. In addition, Hao et al. reported that with the

* Corresponding authors.

E-mail addresses: mkh.leung@cityu.edu.hk (M.K.H. Leung), cehhwang@tsinghua.edu.cn (H. Wang).

<https://doi.org/10.1016/j.apcatb.2023.123365>

Received 10 July 2023; Received in revised form 28 September 2023; Accepted 5 October 2023

Available online 6 October 2023

0926-3373/© 2023 Elsevier B.V. All rights reserved.

size variation of Bi particles from 7.5 to 20 nm, a dramatic change in NRR activity was observed when Bi size was decreased from 20 nm (ammonia yield of $30 \text{ mmol g}^{-1} \text{ h}^{-1}$) to 7.5 nm (ammonia yield of $80 \text{ mmol g}^{-1} \text{ h}^{-1}$) [36]. Meanwhile, MacFarlane et al. synthesized the Bi particles with a size larger than 100 nm, which does not exhibit any measurable electrocatalytic activity for the electroreduction of N_2 to NH_3 [37]. Thus, it follows that a change in particle size can lead to a dramatic change in NRR performance, which may be related to the changes in the reaction mechanisms. Recently, Qiao and Shao proposed a possible two-step reaction pathway for NRR on Bi and Rh catalyst surfaces, which involves an electrochemical process with a two-electron transfer to form N_2H_2 and its subsequent decomposition in the electrolyte producing NH_3 [38,39]. However, rigorous evidence for the proposed two-step reaction pathway is still lacking, and the impact of this pathway on NRR performance and kinetics remains unknown. Furthermore, we speculate that the generation of N_2H_4 and the dramatic NRR activity changes caused by the size changes of Bi particles are related to this reaction pathway.

Focusing on these doubts, in this work, we synthesized multiscale Bi catalysts by tuning the precursor of Bi, giving Bi sizes ranging from nanocrystals (denoted as Bi-3.83 nm and Bi-7.75 nm) to nanoparticles (denoted as Bi-11.70 nm and Bi-17.31 nm). The electrochemical results indicate that Bi nanocrystals (BiNCs) outperform Bi nanoparticles (BiNPs) by approximately an order of magnitude in NH_3 yield rate and 3 times higher in Faradaic efficiency. Then, real-time *in situ* Fourier transform infrared (FTIR) was employed to explore the electrochemical reaction mechanisms on the catalyst surfaces. Interestingly, BiNCs and BiNPs follow different reaction mechanisms to synthesize NH_3 . The BiNPs follow a general associative mechanism for NRR, while the unique two-step reaction mechanism (labelled as dinitrogen desorption mechanism in this work) for NH_3 synthesis can be observed on the BiNCs surfaces that involves an electrochemical process with a two-electron transfer to form N_2H_2 , and that subsequent desorption of N_2H_2 from the catalyst surface to be decomposed in the electrolyte to produce NH_3 . It is worth noting that the undissociated N_2H_2 is further reduced to form N_2H_4 molecules, which explains why N_2H_4 is still generated in some NRR reactions that did not follow the alternating pathway. In addition, the theoretical calculations indicate the dinitrogen desorption pathway involving the transfer of two electrons normally shows lower energy barriers and faster reaction kinetics, resulting in NH_3 production over BiNCs occurring more easily than that over BiNPs, which is consistent with the fact that dramatic changes in NRR performance observed between BiNCs and BiNPs. This work deepens our understanding of the NRR at electrochemical interfaces, shedding new light on developing more advanced NRR catalysts, and the involved *in situ*-FTIR technique can be easily extended into studying other electrochemical reactions.

2. Experimental

2.1. The preparation of catalysts

Carbon black supported BiNPs were synthesized by a modified polyol reduction method, in which the mixture of ethylene glycol (EG) and NaBH_4 serves as the reducing agent for the Bi precursors and carbon black serves the stabilizer for preventing the growth of BiNPs. The compositions of the BiNPs were controlled by regulating the initial Bi precursor ratios. In a typical synthesis of supported BiNPs, 40 mg of carbon support was added to 40 mL of ethylene glycol under ultrasound for 2 h to form carbon black suspension. Next, BiCl_3/EG (20 g L^{-1}) was added dropwise to the suspension under vigorous stirring (0.5 mL of BiCl_3 for Bi-3.83 nm; 0.8 mL of BiCl_3 for Bi-7.75 nm; 1.5 mL of BiCl_3 for Bi-11.70 nm; 2.5 mL of BiCl_3 for Bi-17.31 nm). After stirring for 12 h at room temperature, the pH value of the suspension was adjusted to 11 by adding dropwise a solution of KOH/EG (1 mol/L), and 1 mL of NaBH_4/EG (1 mol/L) was subsequently added to the suspension. Then the temperature of the suspension was heated to 150°C and allowed to

proceed for 2 h under stirring. After the reaction was stopped, the product was separated by centrifugation at 8000 rpm for 20 min, washed with ethanol and doubly distilled water three times each, and dried at 60°C for 24 h under a vacuum.

2.2. Physicochemical characterization

The morphologies and microstructures of the prepared catalysts were characterized by a high-resolution transmission electron microscope (HRTEM, Talos F200X) operated at 200 kV. The X-ray diffraction (XRD) patterns were recorded by a PANalytical X'Pert3 powder X-ray diffractometer, with a $\text{Cu K}\alpha$ radiation (40 kV, 30 mA) of wavelength 0.154 nm. The X-ray photoelectron spectroscopy (XPS) experiments were performed on an X-ray photoelectron spectrometer (Omicron, UHV Multiprobe XP, SPM) using $\text{Al-K}\alpha$ as the exciting source. The concentrations of Bi were measured by inductively coupled plasma atomic emission spectroscopy (ICP-AES). The Bi contents in all the samples were measured by a PerkinElmer 8300 ICP-OES. For obtaining accurate metal compositions, the specimens were diluted by dissolving powder samples in 2% HNO_3 to obtain an ion concentration below 200 ppm.

2.3. Electrochemical tests

All the electrochemical measurements were performed at room temperature using an electrochemical workstation (Gamry) with an H-type cell separated by a pre-treated Nafion 117 membrane (pre-treated by heating in 5% H_2O_2 , 0.5 M H_2SO_4 , and deionized water at 80°C for 1 h, respectively). A standard three-electrode system was used to measure the electrochemical performance, in which synthesized catalysts, $\text{Ag}/\text{AgCl}/\text{sat. KCl}$ and platinum foil ($1 \times 1 \text{ cm}^2$) as the working, reference and counter electrode, respectively. According to the Nernst equation: $E(\text{vs. RHE}) = E(\text{vs. Ag}/\text{AgCl}) + 0.197 + 0.059 \text{ pH}$, all the applied potentials in this work were measured against the $\text{Ag}/\text{AgCl}/\text{sat. KCl}$ and converted to the reversible electrode (RHE). To prepare working electrodes, 130 mg of catalyst (containing 100 mg of carbon black and 30 mg of metal catalyst) was dispersed in a mixed solution of 2 mL of water, 0.7 mL of ethanol and 0.3 mL of 5 wt% Nafion by sonication for at least 30 min to form a homogeneous ink. Then, 100 μL of the as-prepared catalyst ink was loaded onto a carbon cloth ($1 \times 1 \text{ cm}^2$). The electrochemical NRR experiments were conducted in N_2 -saturated 0.5 M K_2SO_4 (pH 3.5), with each compartment containing 60 mL of electrolyte (each was purged with N_2 for at least 30 min to ensure the removal of residual air before each measurement). During the whole electrolysis process, the electrolyte was continuously bubbled with high-purity N_2 (99.999%) with a flow rate of 20 sccm, and was agitated with a stirring bar at a stirring rate of about 500 rpm. Linear sweep voltammetry (LSV) was scanned in the voltage window between -0.7 and 0 V vs. RHE at a rate of 5 mV s^{-1} , and the chronoamperometry tests were operated at different applied potentials (-0.45 , -0.50 , -0.55 , -0.60 , -0.65 , -0.70 V vs. RHE) for 2 h. Before entering the electrolytic cell, the gases were passed through 1 mM H_2SO_4 to remove any possible ammonia or nitrogen oxide pollutants. Then, the gases entered the cathode chamber for nitrogen reduction reaction. Finally, two additional reactors filled with 1 mM H_2SO_4 were connected to the end of the H-cell to capture any undissolved ammonia. It is important to note that all electrochemical cell setups (cells, membrane, flow lines, electrodes, caps) should be thoroughly cleaned with 1 M H_2SO_4 before use, and then soaked in deionized water when not in use.

2.4. Electrochemical *in situ*-FTIR measurement

The electrochemical *in situ* Fourier transform infrared (*in situ*-FTIR) experiments were carried out on a Nicolet iS 50 spectrometers equipped with a liquid nitrogen-cooled MCT-A detector. A ZnSe face-angled crystal with an incident angle 60° was used as a reflection element, with a resolution of 4 cm^{-1} , and was performed for each spectrum. The

pressure-tight H-type cell was used to perform a nitrogen reduction reaction, in which BiNPs were supported on carbon cloth, Ag/AgCl/ sat. KCl and platinum foil ($1 \times 1 \text{ cm}^2$) were used as the working, reference and counter electrodes, respectively. Around 50 mL of 0.5 M K_2SO_4 (pH 3.5) solution was transferred into the spectro-electrochemical cell, which was subsequently assembled into the FTIR optical pathway. The solution was purged with Ar for at least 30 min until two successive interferograms (subsequently collected with a time interval of ~ 2 min) did not show any adsorption difference ($-\log(R_2/R_1)$). Then the FTIR chamber was continuously purged with N_2 at around 50 sccm. For the Chronopotentiometry measurement, the applied potential was set at -0.5 or -0.6 V vs RHE in this experiment. For the linear sweep voltammetry (LSV) measurement, the applied potential was swept between -0.30 V and -0.70 V or -0.20 V and -0.60 V at a scan rate of 1 mV s^{-1} . 126 interferograms were co-added for each spectrum with a collection period of 50 s. Hence each spectrum was the average result of 50 mV interval in LSV.

3. Results and discussion

3.1. Preparation and characterization

Bismuth electrocatalysts with different sizes supported on carbon black were synthesized using a modified polyol reduction method in this work. BiCl_3 was used as the precursor of Bi nanoparticles. Sodium borohydride (NaBH_4) was used as a reducing agent. Ethylene glycol (EG) and carbon black were used as stabilizers and support, respectively. During the reaction, EG could be oxidized to acetate, which could act as a stabilizer for the metal particles. Firstly, bismuth ions are reduced to bismuth atoms by adding reducing reagents; subsequently, the nearby bismuth atoms aggregate at close range. Therefore, increasing the

concentration of BiCl_3 will result in increasing the number of Bi atoms at close range, leading to the average size of the Bi nanoparticles increases. Fig. 1 shows the transmission electron microscopy (TEM) images of the Bi-based nanocatalysts and their corresponding size distributions. The results show that we synthesized Bi nanoparticles with four different mean sizes, denoted as Bi-3.83 nm, Bi-7.75 nm, Bi-11.70 nm and Bi-17.31 nm, and their corresponding Bi contents were determined by inductively coupled plasma atomic emission spectroscopy (ICP-AES) to be 7.35 wt%, 8.48 wt%, 13.1 wt% and 15.60 wt%, respectively. The X-ray diffraction (XRD) patterns confirmed that the as-prepared Bi catalysts crystallized in the rhombohedral phase (space group $R\bar{3}m$) [40, 41]. The broad peak at around 25° is attributed to carbon support (Fig. 1e). Furthermore, the compositions of the Bi particles were analyzed by the X-ray photoelectron spectroscopy (XPS) test, which confirms that four kinds of Bi catalysts are composed of zero valence bismuth elements (Fig. 1f). [42,43].

3.2. Electrochemical N_2 reduction reaction performance

The electrocatalytic performance of the Bi-based catalysts for NRR was measured in a standard H-type cell separated by a proton exchange membrane (Nafion 117) under room temperature and atmospheric pressure. A platinum foil ($1 \times 1 \text{ cm}^2$) and an Ag/AgCl/ sat. KCl was used as the counter- and reference electrodes, respectively. The working electrode was prepared by dispersing metal catalysts onto carbon cloth with a size of $1 \times 1 \text{ cm}^2$. During the whole electrolysis process, the electrolyte was continuously bubbled with high-purity N_2 (99.999%) with a flow rate of 20 sccm. For a quantitative assessment of electrochemical NH_3 production, colorimetric assay (indophenol blue method) was explored, while the potential by-product of hydrazine (N_2H_4) was evaluated by the Watt and Chrisp approach. Their corresponding

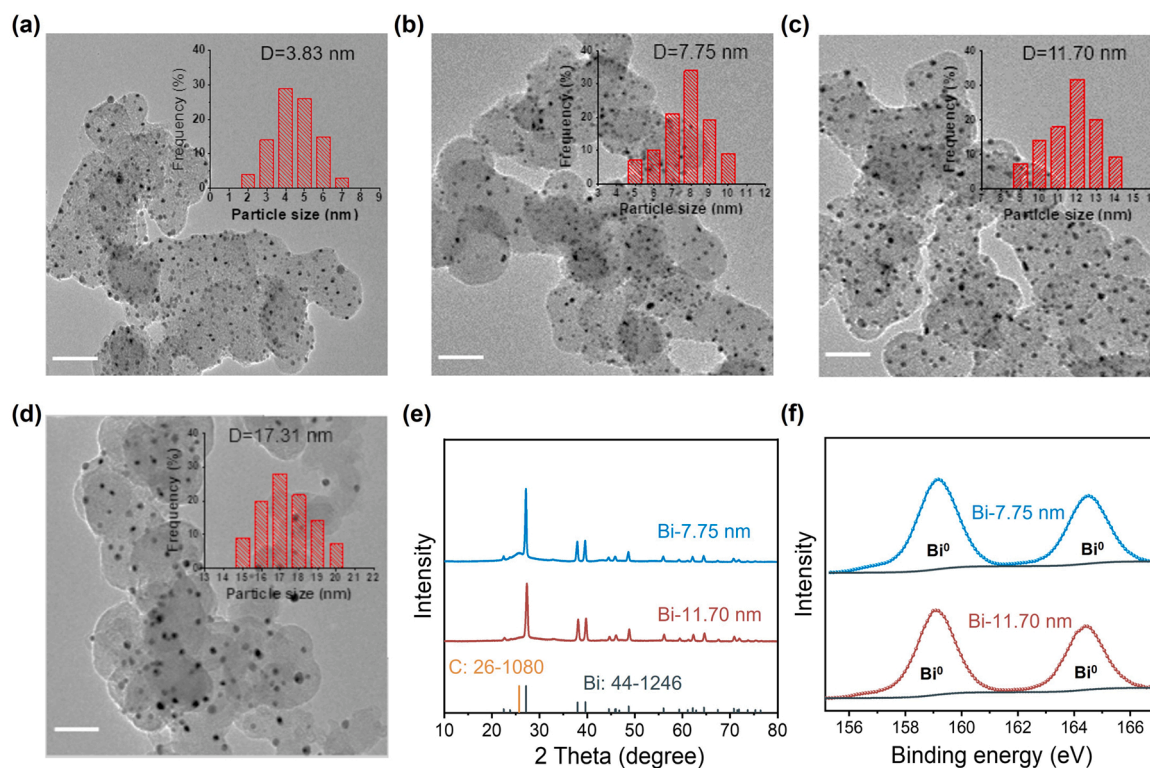


Fig. 1. Morphology and structure characterizations. (a) Transmission electron microscopy (TEM) images for the as-obtained Bi-3.83 nm (Bi anchored on carbon black), and corresponding Bi size distribution (mean size: 3.83 nm). Scale bar: 50 nm. (b) Transmission electron microscopy (TEM) images for the as-obtained Bi-7.75 nm (Bi anchored on carbon black), and corresponding Bi size distribution (mean size: 7.75 nm). Scale bar: 50 nm. (c) Transmission electron microscopy (TEM) images for the as-obtained Bi-11.70 nm (Bi anchored on carbon black), and corresponding Bi size distribution (mean size: 11.70 nm). Scale bar: 50 nm. (d) Transmission electron microscopy (TEM) images for the as-obtained Bi-17.31 nm (Bi anchored on carbon black), and corresponding Bi size distribution (mean size: 17.31 nm). Scale bar: 50 nm. (e) XRD patterns of the Bi-7.75 nm and Bi-11.70 nm. (f) XPS patterns of the Bi-7.75 nm and Bi-11.70 nm.

calibration curves are depicted in Fig. S1. We initially performed linear sweep voltammetry (LSV) tests in an Ar/N₂-saturated electrolyte to qualitatively distinguish current density for four sizes of Bi catalysts and estimate the activity of NRR. As shown in Fig. 2a and Fig. S2, the current density of Bi-3.83 nm is superior to that of other typical Bi-based catalysts with larger particle sizes, and the maximum current density gap is observed between Bi-7.75 nm and Bi-11.70 nm. Next, we conducted a series of chronoamperometry (CA) measurements for all sizes of Bi catalysts at different applied potentials to examine the electroproduction of NH₃ yield and Faradaic efficiency. Notably, the highest activity and selectivity on Bi-based catalysts can be detected on the Bi-3.83 nm surface at -0.50 V vs. RHE with the ammonia yield rate of $404.9 \text{ ug h}^{-1} \text{ mg}_{\text{Bicat}}^{-1}$ and corresponding Faradaic efficiency of 62.37% (Fig. 2b and Fig. S3). In comparison, Bi-17.31 nm offered the lowest NH₃ yield rate ($63.7 \text{ ug h}^{-1} \text{ mg}_{\text{Bicat}}^{-1}$) and Faradaic efficiency (19.59%) at -0.60 V vs. RHE (Fig. 2c and Fig. S4). It is worth noting that Bi-7.75 nm outperforms Bi-11.70 nm by approximately an order of magnitude in NH₃ yield rate and 3 times higher in Faradaic efficiency, while only a small change in NRR activity can be detected between Bi-3.83 nm and Bi-7.75 nm ($302.4 \text{ ug h}^{-1} \text{ mg}_{\text{Bicat}}^{-1}$; 58.80%) catalysts, as well as between Bi-11.70 nm ($85.30 \text{ ug h}^{-1} \text{ mg}_{\text{Bicat}}^{-1}$; 23.23%) and Bi-17.31 nm catalysts (Fig. S5–S7), which is consistent with the corresponding current density change. More details about the composition and catalytic performance over as-synthesized Bi catalysts are summarized in Table S1. To avoid that the catalysts cannot continue for sufficient time for ammonia productivity, we performed long-time NRR measurements on Bi-based catalysts. As shown in Fig. S8, four sizes of Bi catalysts show a negligible decrease in ammonia yield after 12 h of NRR operation. To verify the deduction that the measured NH₃ comes indeed from electrochemical NRR rather than from any nitrogenous contaminants from the environment (e.g., membrane, cell, nitrogen gas, laboratory), additional control experiments, including Ar-saturated electrolyte, bare carbon cloth without catalyst, open circuit, or electrolyte placed in the air for 24 h were carried out. All results demonstrate that there is no detectable

NH₃ production (Fig. S9 and Fig. S10). To further confirm the origin of NH₃, isotope labelling experiments were performed for Bi-7.75 nm and Bi-11.70 nm catalysts by using ¹⁵N₂ as the feeding gas, and all of the ¹H nuclear magnetic resonance (NMR) spectra show doublet peaks with the coupling constants of 73.0 Hz (Fig. S11), assigned to the typical ¹⁵NH₄⁺ signals. These results confirm that the detected NH₃ was really produced from the electrochemical reduction of N₂. Another interesting phenomenon worth noting is that both Bi-3.83 nm and Bi-7.75 nm exhibit Faradaic efficiency of about 2% for N₂H₄ at -0.50 V vs. RHE, while no N₂H₄ can be detected for the Bi-11.70 nm and Bi-17.31 nm at all the applied potentials (Fig. 2d), explaining the possibility of dinitrogen desorption mechanism occurring on Bi-3.83 nm and Bi-7.75 nm.

In addition, the electrochemically active surface area (ECSA) is an important parameter when investigating the electrocatalytic activity of catalysts. For the NRR, the ECSA can be evaluated based on the double-layer capacitance (C_{dl}) at the interface between electrolyte and the electrode. In this work, a series of cyclic voltammetry (CV) measurements were conducted at different scan rates in the range of 0.1–0.2 V (vs. RHE). The corresponding C_{dl} values can be calculated using the formula: $i_{\text{c}} = v \times C_{\text{dl}}$, which is equal to the slope of the linear relationship between the current density and the scan rate of the CV curves. As depicted in Fig. S12, Bi-3.83 nm exhibits a higher C_{dl} value (40 mF cm^{-2}) than Bi-7.75 nm (37 mF cm^{-2}), Bi-11.70 nm (33 mF cm^{-2}) and Bi-17.31 nm (27 mF cm^{-2}), indicating that the Bi-3.83 nm catalyst has the largest electrochemically active surface area.

3.3. Reaction mechanisms on the BiNPs and BiNCs

To explore the reasons for the dramatic change exhibited by Bi-7.75 nm and Bi-11.70 nm on NRR, electrochemical *in situ* Fourier transform infrared spectroscopy (*in situ*-FTIR) was conducted as illustrated in Fig. 3a (measured in a gas-tight H-type FTIR electrochemical cell with a three-electrode configuration under ambient conditions), which is a powerful tool to analyze the complex reaction mechanism by

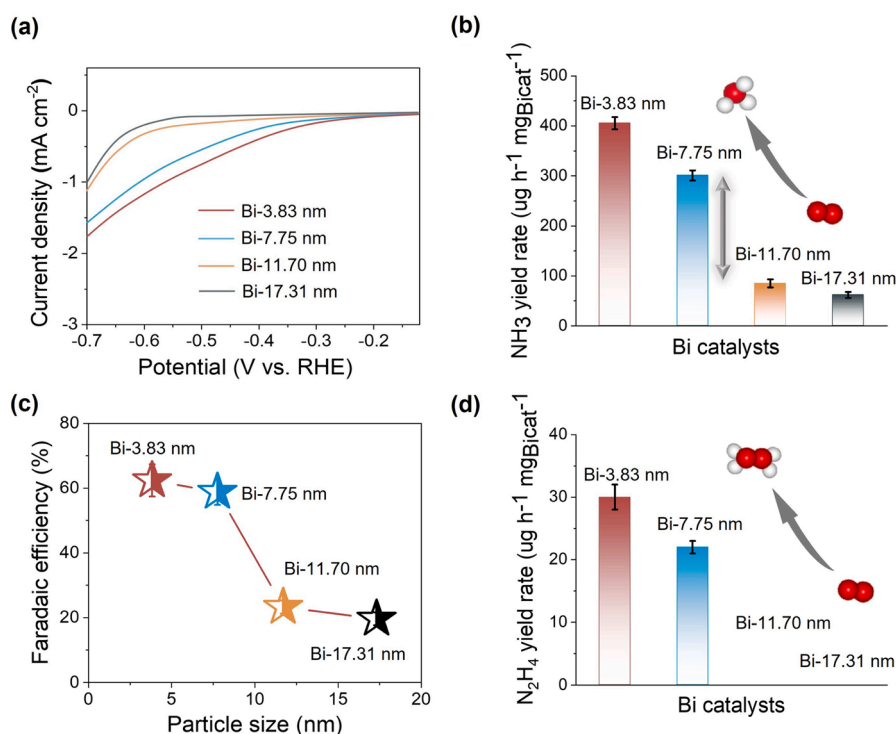


Fig. 2. ENRR performance for Bi-based nanocatalysts (including Bi-3.83 nm, Bi-7.75 nm, Bi-11.70 nm and Bi-17.31 nm) in N₂-saturated electrolytes (0.5 M of K₂SO₄, pH 3.5). (a) N₂-saturated LSV curves over the as-obtained Bi catalysts with four particle sizes. Scan rate: 5 mV s^{-1} . (b) NH₃ yield rates over the as-obtained Bi catalysts with four particle sizes. (c) NH₃ Faradaic efficiencies over the as-obtained Bi catalysts with four particle sizes. (d) N₂H₄ yield rates over the as-obtained Bi catalysts with four particle sizes.

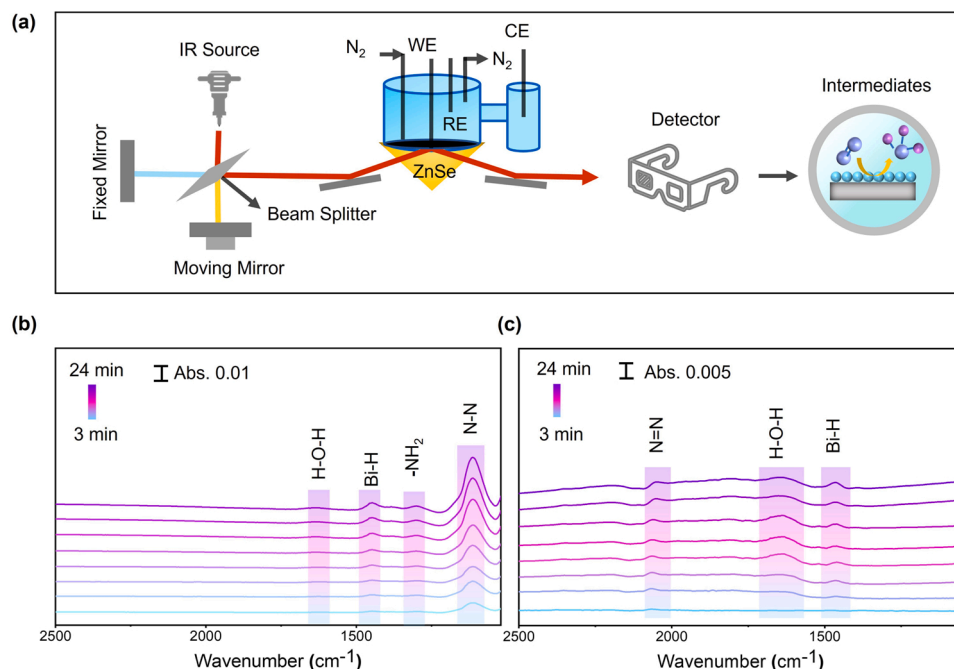


Fig. 3. *In situ*-FTIR measurements. (a) Schematic illustration of FTIR configurations for studies on nanocatalysts. A ZnSe face-angled crystal with incident angle 60° was used as reflection element, with a resolution of 4 cm^{-1} , were performed for each spectrum. (b) Electrochemical *in situ*-FTIR spectra of the NRR on the Bi-11.70 nm at -0.6 V vs. RHE. (c) Electrochemical *in situ*-FTIR spectra of the NRR on the Bi-7.75 nm at -0.5 V vs. RHE.

monitoring the presence and identities of intermediates. Firstly, the time-resolved *in situ*-FTIR spectra were collected on the Bi surface during the chronoamperometry scan in an N_2 -saturated electrolyte for 1440 s, where the time interval between two successive spectra is 180 s. The band assignments are summarized in Table S2. As for the Bi-11.70 nm (Fig. 3b), it is clear that two obvious absorption signals at 1117 and 1301 cm^{-1} can be observed assigned to N-N stretching and $-\text{NH}_2$ wagging, respectively [44]. The peak intensity increases with the extension of reaction time, demonstrating more active sites are gradually involved in the catalytic breakage of the $\text{N}\equiv\text{N}$ triple bonds and the production of $-\text{N}_2\text{H}_y$ ($1 \leq y \leq 4$) species on the electrode surface. Additional minor adsorption bands located at 1380 cm^{-1} correspond to the asymmetric deformation vibration of $\delta_{\text{as}}\text{NH}_4^+$ generated during the nitrogen reduction reaction [45,46]. In addition, the bands at 3353 cm^{-1} and 1636 cm^{-1} were assigned to the O-H stretching and H-O-H bending vibrations, respectively, of the first-layer water. Simultaneously, a broad positive band at $\sim 1445\text{ cm}^{-1}$ (Bi-H) that was obtained is attributed to the coexistence of competing HER [47]. These signals can be clearly revealed in a single spectrum shown in Fig. S13, and this result demonstrates that the NRR on Bi-11.70 nm follows an associative mechanism. Specially, as shown in Fig. 4a, the dissolved N_2 molecules can be initially adsorbed by the Bi surface sites on the catalyst surfaces. Then, the activated H^+ favours forming a highly stable $-\text{N}\equiv\text{N}-\text{H}$ bond, which can accelerate the dissociation of the $\text{N}\equiv\text{N}$ bond. Next, another H^+ hydrogenates the weakened $-\text{N}\equiv\text{N}-\text{H}$ to form a $-\text{H}-\text{N}=\text{N}-\text{H}$ bond; thereafter, a free NH_3 molecule associated with the adsorbed $-\text{NH}_2$ is generated by continuous electron transfer and hydrogenation. Finally, the second NH_3 molecule is obtained by adding the H^+ and electron to $-\text{NH}_2$, indicating that a complete nitrogen reduction reaction is achieved on the Bi-11.70 nm surface under ambient temperature and normal atmospheric pressure.

By comparison, the time-resolved *in situ*-FTIR spectra were also collected on the Bi-7.75 nm surface under the same conditions. Interestingly, different peak positions were observed during the NRR. As shown in Fig. 3c, except for the three peaks of O-H stretching (3353 cm^{-1}), H-O-H bending vibrations (1636 cm^{-1}) and adsorbed H atoms (1445 cm^{-1}), an obvious band at 2070 cm^{-1} assigned to the

$\text{N}=\text{N}$ stretching of end-on adsorbed N_2H_x ($0 \leq x \leq 2$) was observed that have never been detected on the Bi-11.70 nm catalyst [48], and the intensity increases with electrolysis time. These signals can be clearly revealed in a single spectrum shown in Fig. S14. To confirm the $\text{N}=\text{N}$ stretching band belongs to N_2H_x rather than contaminants, the FTIR spectrum of Bi-7.75 nm in an Ar-saturated electrolyte was also collected. In contrast, no ammonia-related fragments can be detected, and all the signals are assigned to H_2O in the electrolyte and adsorbed H atoms on the catalyst surface (Fig. S15). Similarly, possible byproducts were also quantified (Fig. S16) at -0.50 V . The Bi-7.75 nm exhibited a Faradaic efficiency of 58.8% for NH_3 , 39.31% for H_2 and 1.89% for N_2H_4 . These results confirm that Bi-7.75 nm are the same as Bi-11.70 nm, with NH_3 being the major product of NRR, but different intermediates were detected on the catalyst surfaces. After that, we analyzed the possible reaction mechanism for the nitrogen reduction on the Bi-7.75 nm. It is worth noting that only the adsorbed N_2H_x ($0 \leq x \leq 2$) can be detected on the electrode surface of Bi-7.75 nm during the NRR, no peaks related to the existence of $-\text{NH}_x$ and N-N bonds, which reveals that the formed N_2H_2 might more easily desorb from the Bi-7.75 nm surface rather than further reduction. In addition, it is well known that the N_2H_2 is unstable and easily spontaneous decomposes into NH_3 and N_2 under ambient conditions, resulting in the conversion of N_2H_2 to NH_3 occurs in the electrolyte (Fig. S17), which is consistent with the *in situ*-FTIR results. Therefore, the dinitrogen desorption pathway for the nitrogen reduction reaction is detected on the bismuth nanocrystals surface (Fig. 4b), that is the adsorbed N_2 molecule on edge or defective sites first reduces to $^*\text{N}_2\text{H}_2$ by a two-electron transfer process which immediately desorbs from the Bi-7.75 nm surface and decomposes into NH_3 and N_2 ($3\text{ N}_2\text{H}_2 \rightarrow 2\text{NH}_3 + 2\text{N}_2$). However, the possibility of N_2H_2 dissociation or its further reduction cannot be completely ruled out, which involves the sequential hydrogenation on the outer N atom to form N_2H_4 molecules, which explains why N_2H_4 can be only detected on the Bi-7.75 nm surface, being consistent with the experimental results.

Then, we also applied the same *in situ*-FTIR analysis for Bi-3.83 nm and Bi-17.31 nm catalysts. As shown in Fig. S18, the peaks of the N-N stretching, $-\text{NH}_2$ wagging and $\delta_{\text{as}}\text{NH}_4^+$ vibration can be detected on the Bi-17.31 nm surfaces, indicating that the Bi-17.31 nm and Bi-11.70 nm

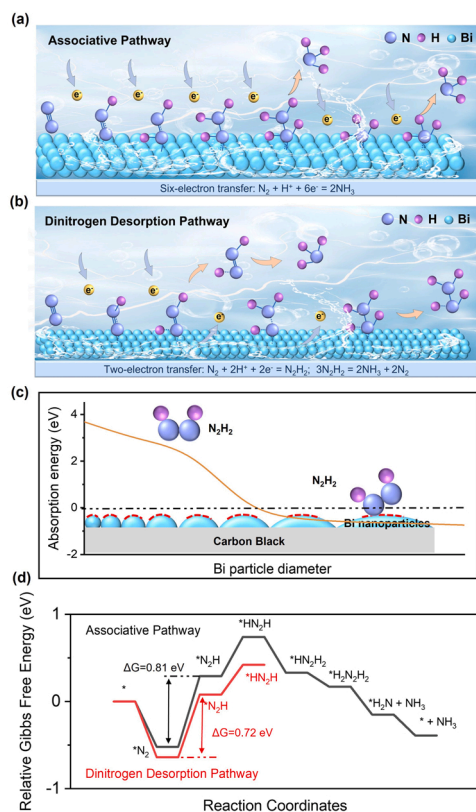


Fig. 4. Reaction mechanisms and DFT calculations. (a) BiNPs follows an associative mechanism (a six-electron transfer process). (b) BiNPs follows a dinitrogen desorption mechanism (a two-electron transfer process). Immediately after N_2H_2 desorbs from the BiNCs surface, it decomposes into ammonia and nitrogen ($3 N_2H_2 \rightarrow 2NH_3 + 2 N_2$). (c) The adsorption energies of N_2H_2 on a series of Bi nanoparticles with different diameters. (d) The Gibbs free energy of each hydrogenation intermediate during NRR process on the BiNCs (following dinitrogen desorption pathway) and BiNPs (following associative pathway) surface.

catalysts follow the same associative mechanism for the NRR. As for the Bi-3.83 nm surfaces, an obvious band of N = N stretching can be generated during the ammonia synthesis, revealing that Bi-3.83 nm and Bi-7.75 nm catalysts follow the same NRR mechanism (Fig. S19).

3.4. DFT calculation

The above *in situ*-FTIR results confirm that the N_2H_2 adsorption behavior plays a decisive role in determining the electrochemical NRR pathway. To unravel the relationship of N_2H_2 adsorption on Bi nanoparticle size, we calculated the adsorption energies of N_2H_2 on a series of Bi nanoparticles with different diameters via density functional theory (DFT) simulation. To simulate the surface reaction, we constructed the slab models to simulate surfaces with different curvatures (Fig. S20 and Fig. S21), and the detailed derivation formula of the spherical equation is shown in the supporting information. As shown in Fig. 4c and Table. S3, the computed N_2H_2 adsorption energies (E_{abs}) clearly exhibit a negative proportional dependence on Bi sizes effective particle diameter, and N_2H_2 can be desorbed from the catalyst surface as the adsorption energy shows a positive value when particle size is decreased. This phenomenon is consistent with the observed experimental results: i) small-sized Bi particles have a larger radius of curvature, allowing N_2H_2 to desorb from the Bi catalyst surface, which determines the change of the NRR path; ii) when the particle size is less than 7.75 nm, N_2H_2 can be desorbed from the catalyst surface, therefore following the dinitrogen desorption pathway; iii) when the particle size

is larger than 11.70 nm, N_2H_2 cannot be desorbed from the catalyst surface and will continue to complete the hydrogenation process to form NH_3 .

Moreover, the Gibbs free energy of each hydrogenation intermediate during NRR process on the BiNCs (following dinitrogen desorption pathway) and BiNPs (following associative pathway) surface were calculated and plotted the corresponding diagrams with the lowest energy barrier (Fig. 4d). In particular, based on the above experimental analysis results, we constructed the curved surface models for the BiNCs system and the flat surface models for the BiNPs systems (Fig. S22 and Fig. S23). Notably, the results show that the hydrogenation step ($*N_2$ to $*N_2H$) is the rate-determining step for both of the catalysts, while the BiNCs following the dinitrogen desorption pathway exhibit a lower energy barrier with 0.72 eV compared to that employing the BiNPs. The above findings explain that the BiNCs facilitate the NRR by lowering the energy barrier for the rate-determining step, in consistence with the experimental results.

The above experimental and analytical studies on BiNCs and BiNPs have confirmed that (1) the dramatic change in NRR performance between Bi-7.75 nm and Bi-11.70 nm is attributed to the change of NRR pathway induced by the different particle sizes; (2) Bi particles with the size of smaller than 7.75 nm preferentially undergo the dinitrogen desorption pathway rather than the associative pathway to synthesize NH_3 , in agreement with the high N_2 reaction rate and Faradaic efficiency displayed and the detection of N_2H_4 in NRR; (3) In comparison with the associative pathway (i.e., six-electron processes), the dinitrogen desorption pathway involving the two electrons transfer normally shows lower energy barriers and faster reaction kinetics, enabling the delivery of a larger current density for the electrochemical NRR on the BiNCs surface. Therefore, we can infer that the dinitrogen desorption pathway reaction mechanism, as a newly proposed mechanism, can significantly promote the NRR performance of the catalyst. These findings not only deepen our understanding of the nitrogen reduction reaction and sheds new light on the development of more advanced NRR catalysts but also explain the reasons for the generation of N_2H_4 and why a minute change in the catalyst structure would cause a dramatic change in activity. Furthermore, we should devote more attention to it in the future and explore its reaction process and influencing factors to better control the electrochemical reaction pathway by changing the size, morphology and composition of the catalyst.

3.5. The dependence of applied potential on NRR performance revealed by *in situ*-FTIR

The real-time *in situ*-FTIR spectra were collected during a Linear sweep voltammetry (LSV) scan of the BiNPs surface in N_2 -saturated electrolyte from -0.30 to -0.70 V and are shown in Fig. 5a. Clearly, no absorption band can be observed until the potential reaches about -0.35 V, in good accordance with the electrochemical result that no NH_3 was generated between -0.30 V and -0.35 V. It should be noted that the corresponding linear scanning voltammogram in Fig. S24 exhibits that the current density is lower than that of BiNPs operating in a standard H-type cell (Fig. 2a), which is mainly due to the position modulation of the working electrode in an FTIR H-type cell. Moreover, the intensities of the peaks including N-N stretching, $-NH_2$ wagging, and $\delta_{as}NH_4^+$ vibration reached the maximum at -0.6 V and then gradually decreased. In contrast, the intensity of the Bi-H signal always increases with the applied potential, which was possibly caused by the HER becoming the dominant reaction at the cathode. Intriguingly, the results detected by *in situ*-FTIR are consistent with the electrochemical results obtained in the standard H-cell. The electro-chemical NRR obtains the highest activity and selectively at the potential of -0.6 V vs. RHE, and as the applied potential becomes more negative, both NH_3 yield rate and corresponding Faradaic efficiency decrease considerably.

The same *in situ*-FTIR tests were also performed on the Bi-7.75 nm surface from -0.20 V to -0.60 V, and the corresponding LSV curve

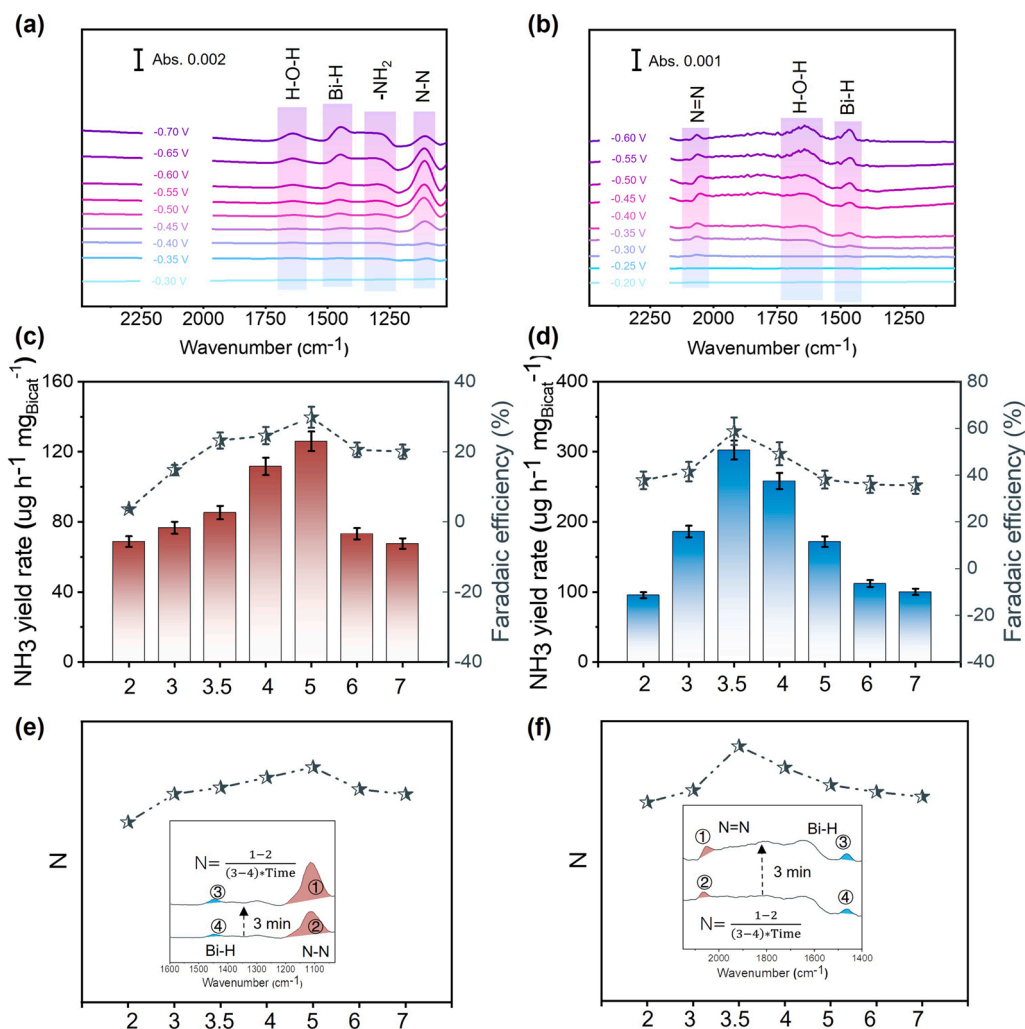


Fig. 5. The dependence of applied potential and pH on NRR performance. (a) The FTIR spectra collected during a LSV scan from -0.30 to -0.70 V on the Bi-11.70 nm surface. (b) The FTIR spectra collected during a LSV scan from -0.20 to -0.60 V on the Bi-7.75 nm surface. (c) NH₃ yield rates and Faradaic efficiencies of Bi-11.70 nm at different pH electrolytes. (d) NH₃ yield rates and Faradaic efficiencies of Bi-7.75 nm at different pH electrolytes. (e) The ratio of the band area changes rates between the N=N stretching and hydrogen adsorbed on Bi-11.70 nm at different pH electrolytes. (f) The ratio of the band intensities between the N=N stretching and hydrogen adsorbed on Bi-7.75 nm at different pH electrolytes.

indicated that a higher current density could be detected compared with Bi-7.75 nm (Fig. S25). Fig. 5b shows the *in situ*-FTIR results, where no absorption band can be observed until the overpotential reaches -0.25 V, suggesting the decreased energy barrier to trigger the reaction as well as the improved NRR kinetic processes on the Bi-7.75 nm. Then, the peak intensity of the N=N stretching increases with the applied potential and obtains a maximum at -0.5 V, after which the peak starts to decrease with the continued increase of the Bi-H signal. Similarly, all *in situ*-FTIR results obtained on the Bi-7.75 nm surfaces are consistent with the electrochemical NRR tests, that the highest activity and selectivity obtained at the potential of -0.5 V, and as the applied potential becomes more negative, both NH₃ yield rate and corresponding Faradaic efficiency decrease considerably. The above results confirm that the *in situ*-FTIR tests can be used as an accurate tool to verify the electrochemical test results, which can measure the onset potential and the optimal active potential of NRR, as well as the dependence of applied potential on NRR or HER performance. In addition, we know that ammonia is ubiquitous in all aqueous solutions and on many surfaces due to its polarity and high-water solubility, and rigorous control experiments and validation tests are required to exclude ammonia contamination when conducting NRR testing. Therefore, *in situ*-FTIR test may potentially serve as a verification method to confirm the origin of

ammonia products by detecting NRR intermediates.

3.6. The dependence of electrolyte pH values on NRR performance revealed by *in situ*-FTIR

In addition to the intrinsic activities of catalysts, the variation in the pH values of electrolytes would also change the NRR activity and selectivity, and thus we performed electrochemical NRR tests at different pH values to evaluate the effects of hydrogen ion concentrations. As shown in Fig. 5c and d, the result suggests that the optimized NRR performances of the Bi-11.70 nm and Bi-7.75 nm catalysts can be obtained in acidic electrolytes of pH 5 and pH 3.5, respectively. That suggests that an appropriate concentration of hydrogen ion could significantly facilitate the NRR performance on catalysts, mainly attributed to the fact that pH value has a different kinetic effect on HER and NRR. The kinetics of the HER at high pH values (lack of sufficient protons) is relatively lower in comparison to the low pH value; however, the NRR performance in high pH value is not very high. Therefore, at high pH values (pH>5 for Bi-11.70 nm; pH>3.5 for Bi-7.75 nm), the rate of the NRR would be limited due to the too-confined access to protons for the protonation of nitrogen species, while at low pH values (pH<5 for Bi-11.70 nm; pH<3.5 for Bi-7.75 nm), the competition from the HER

would be overwhelming and would simultaneously suppress the NRR. The Bi-7.75 nm exhibits the best activity and selectivity at a lower pH value than that of Bi-11.70 nm, which is consistent with the fact that better NRR activity requires more hydrogen ions. The pH effects on NRR performance can be confirmed by *in situ*-FTIR test as well because the ratio of the signal coverage (peaks area) between NRR and HER varies with the applied pH values. In this work, the time-resolved *in situ*-FTIR tests were performed on the Bi-7.75 nm and Bi-11.70 nm surfaces at each applied pH value. The inset of Fig. 5e shows the FTIR spectra obtained at the third and sixth minutes when we performed the NRR test on Bi-11.70 nm surfaces at pH 5, and the N value can be calculated by measuring the rate ratio of the N-N/ Bi-H band area with time. Therefore, the N value at other pH values can be obtained by the same strategy, as summarized in Table S4. Interestingly, the trend of N value with pH value is consistent with the trend of Faradaic efficiency with pH value obtained during electrochemical NRR tests, which suggests that N value may be used as a quantity to evaluate the NRR selectivity. Similarly, as for the Bi-7.75 nm catalysts, the N value changes with different pH values in the electrolyte can be achieved by measuring the rate ratio of the Bi-H/N = N band area with time (Fig. 5f), which is also consistent with the electrochemical NRR test results, illustrating that our above-established N value calculation formula is still reliable.

The N value at other pH values can be obtained by the same strategy, as summarized in Table S5. The above results confirm that *in situ*-FTIR experiments can be used to analyze the relationship between NRR activity and applied pH by detecting the coverage changes of the N-N (associative mechanism), N = N (dinitrogen desorption mechanism) and Bi-H (competing HER) peaks. It is worth noting that the N-value calculation method first proposed in this work is expected to serve as an innovative technology to analyze the activity and the Faradaic efficiency of the catalysts under different reaction conditions because it is independent of the NRR reaction pathways. This calculation principle should also be applied to other electrochemical fields (OER, ORR, etc.).

4. Conclusions

In summary, this work presents a comparative investigation of the nitrogen reduction process on Bi catalyst surfaces with different particle sizes. A new mechanism, namely, the dinitrogen desorption mechanism, for NRR has been highlighted, which may explain some intriguing phenomena reported in previous experimental works. The experimental results indicate that the small-size effect of Bi catalysts enables weak N₂H₂ adsorption on catalysts to drive the N₂ reduction reaction with a dinitrogen desorption mechanism involving the transfer of two electrons driving, which results in NH₃ production over BiNCs to occur more easily than that over BiNPs. Furthermore, our results confirm that *in situ*-FTIR not only can be used as an accurate tool to verify the electrochemical test results but also can directly reveal the intricate interplay between selectivity-determining factors in Bi-based NRR, such as applied potential and electrolyte pH. The use of state-of-the-art *in situ*-FTIR gives new impetus to the *in situ* characterization of a broader class of catalytic materials under relevant reaction conditions. It stimulates comprehensive theoretical investigations on size effect- and reaction route-induced restructuring. This work deepens our understanding of the nitrogen reduction reaction at electrocatalytic interfaces and sheds new light on developing more advanced NRR catalysts.

CRediT authorship contribution statement

Conceptualization, H.W. and M.K.H.L.; Methodology, H.W., M.K.H.L. and X.L.; Investigation, X.L., J.L., G.C. and J.Z.; Writing – Original Draft, X.L.; Writing – Review & Editing, H.W., G.C. and X.L.; Funding Acquisition, H.W. and M.K.H.L.; Software, G.H.; Supervision, H.W. and M.K.H.L. X. L and G. H contributed equally to this work. All authors discussed the results and commented on the manuscript.

Declaration of Competing Interest

The authors declare that they have no known competing financial interests or personal relationships that could have appeared to influence the work reported in this paper.

Data Availability

Data will be made available on request.

Acknowledgements

We gratefully acknowledge the funding from the National Key Research and Development Program of China (Grant No. 2022YFB4002602), Natural Science Foundation of China (Grant No. 22138005), the Research Grants Council of the Hong Kong Special Administrative Region, China (Project No. CityU 11206520), Ningbo Municipal Government Innovation 2025 Scheme (No. 2018B10023) and the Shenzhen Knowledge Innovation Program (Basic Research, JCYJ20190808181205752).

Appendix A. Supporting information

Supplementary data associated with this article can be found in the online version at doi:10.1016/j.apcatb.2023.123365.

References

- [1] J.W. Erisman, J. Galloway, M.A. Sutton, Z. Klimont, Z. Winiwarter, How a century of ammonia synthesis changed the world, *Nat. Geosci.* 1 (2008) 636–639.
- [2] F. Jiao, B. Xu, Electrochemical ammonia synthesis and ammonia fuel cells, *Adv. Mater.* 31 (2019), e1805173.
- [3] G. Marnellos, M. Stoukides, Ammonia synthesis at atmospheric pressure, *Science* 282 (1998) 98–100.
- [4] H. Chen, J. Liang, K. Dong, L. Yue, T. Li, Y. Luo, Z. Feng, N. Li, M.S. Hamdy, A. A. Alshehri, Y. Wang, X. Sun, Q. Liu, Ambient electrochemical N₂-to-NH₃ conversion catalyzed by TiO₂ decorated Juncus effusus-derived carbon microtubes, *Inorg. Chem. Front.* 9 (2022) 1514–1519.
- [5] H.R. Bryan, K.M. Suryanto, J. Choi, Y.H. Rebecca, H. Du, A.N. Simonov, D. R. MacFarlane, Nitrogen reduction to ammonia at high efficiency and rates based on a phosphonium proton shuttle, *Science* 372 (2021) 1187–1191.
- [6] M. Wang, M.A. Khan, I. Mohsin, J. Wicks, A.H. Ip, K.Z. Sumon, C. Dinh, E. H. Sargent, I.D. Gates, M.G. Kibria, Can sustainable ammonia synthesis pathways compete with fossil-fuel based haber–bosch processes? *Energy Environ. Sci.* 14 (2021) 2535–2548.
- [7] G.F. Chen, A. Savateev, Z. Song, H. Wu, Y. Markushyna, L. Zhang, H. Wang, M. Antonietti, Saving the energy loss in lithium-mediated nitrogen fixation by using a highly reactive Li₃ N intermediate for C–N coupling reactions, *Angew. Chem. Int. Ed.* 61 (2022), e202203170.
- [8] W. Wang, H. Zhou, Y. Liu, S. Zhang, Y. Zhang, G. Wang, H. Zhang, H. Zhao, Formation of B₁₀C coordination to stabilize the exposed active nitrogen atoms in g-C(3) N(4) for dramatically enhanced photocatalytic ammonia synthesis performance, *Small* 16 (2020), e1906880.
- [9] S. Zhang, Y. Zhao, R. Shi, C. Zhou, G.I.N. Waterhouse, Z. Wang, Y. Weng, T. Zhang, Sub-3 nm ultrafine Cu(2) O for visible light driven nitrogen fixation, *Angew. Chem. Int. Ed.* 60 (2021) 2554–2560.
- [10] W. Gao, J. Guo, P. Wang, Q. Wang, F. Chang, Q. Pei, W. Zhang, L. Liu, P. Chen, Production of ammonia via a chemical looping process based on metal imides as nitrogen carriers, *Nat. Energy* 3 (2018) 1067–1075.
- [11] L.F. Gao, Y. Cao, C. Wang, X.W. Yu, W.B. Li, Y. Zhou, B. Wang, Y.F. Yao, C.P. Wu, W.J. Luo, Z.G. Zou, Domino effect: gold electrocatalyzing lithium reduction to accelerate nitrogen fixation, *Angew. Chem. Int. Ed.* 60 (2021) 5257–5261.
- [12] Y. Fang, Y. Xue, Y. Li, H. Yu, L. Hui, Y. Liu, C. Xing, C. Zhang, D. Zhang, Z. Wang, X. Chen, Y. Gao, B. Huang, Y. Li, Graphdiyne interface engineering: highly active and selective ammonia synthesis, *Angew. Chem. Int. Ed.* 59 (2020) 13021–13027.
- [13] H. Cheng, P. Cui, F. Wang, L.X. Ding, H. Wang, High efficiency electrochemical nitrogen fixation achieved with a lower pressure reaction system by changing the chemical, *Equilib.*, *Angew. Chem. Int. Ed.* 58 (2019) 15541–15547.
- [14] S.Z. Andersen, V. Colic, S. Yang, J.A. Schwalbe, A.C. Nielander, J.M. McEnaney, K. Enemark-Rasmussen, J.G. Baker, A.R. Singh, B.A. Rohr, M.J. Statt, S.J. Blair, S. Mezzavilla, J. Kibsgaard, P.C.K. Vesborg, M. Cargnello, S.F. Bent, T.F. Jaramillo, I.E.L. Stephens, J.K. Nørskov, I. Chorkendorff, A. Rigorous, Electrochemical ammonia synthesis protocol with quantitative isotope measurements, *Nature* 570 (2019) 504–508.
- [15] H. Zou, W. Rong, S. Wei, Y. Ji, L. Duan, Regulating kinetics and thermodynamics of electrochemical nitrogen reduction with metal single-atom catalysts in a pressurized electrolyser, *Proc. Natl. Acad. Sci. U. S. A.* 117 (2020) 29462–29468.

- [16] H. Wang, Y. Li, C. Li, K. Deng, Z. Wang, Y. Xu, X. Li, H. Xue, L. Wang, One-pot synthesis of bi-metallic pdru tripods as an efficient catalyst for electrocatalytic, Nitrogen Reduct. Ammon., J. Mater. Chem. A 7 (2019) 801–805.
- [17] M.A. L  gar  , G.B. Chabot, R.D. Dewhurst, E. Welz, I. Krummenacher, B. Engels, H. Braunschweig, Nitrogen Fixation and Reduction at Boron, Science 359 (2018) 896–900.
- [18] Y.T. Liu, D. Li, J. Yu, B. Ding, Stable confinement of black phosphorus quantum dots on black tin oxide nanotubes: a robust, double-active electrocatalyst toward efficient nitrogen fixation, Angew. Chem. Int. Ed. 58 (2019) 16439–16444.
- [19] X. Liu, H. Jang, P. Li, J. Wang, Q. Qin, M.G. Kim, G. Li, J. Cho, Antimony-based composites loaded on phosphorus-doped carbon for boosting faradaic efficiency of the electrochemical nitrogen reduction reaction, Angew. Chem. Int. Ed. 58 (2019) 13329–13334.
- [20] R. Zhang, S. Zhang, Y. Guo, C. Li, J. Liu, Z. Huang, Y. Zhao, Y. Li, C. Zhi, A. Zn–Nitrite, battery as an energy-output electrocatalytic system for high-efficiency ammonia synthesis using carbon-doped cobalt oxide nanotubes, Energy Environ. Sci. 15 (2022) 3024–3032.
- [21] Y. Ren, C. Yu, X. Tan, H. Huang, Q. Wei, J. Qiu, Strategies to suppress hydrogen evolution for highly selective electrocatalytic nitrogen reduction: challenges and perspectives, Energy Environ. Sci. 14 (2021) 1176–1193.
- [22] G. Qing, T.W. Hamann, New electrolytic devices produce ammonia with exceptional selectivity, Joule 3 (2019) 634–636.
- [23] J. Long, S. Chen, Y. Zhang, C. Guo, X. Fu, D. Deng, J. Xiao, Direct electrochemical ammonia synthesis from nitric oxide, Angew. Chem. Int. Ed. 59 (2020) 9711–9718.
- [24] N. Lazouski, M. Chung, K. Williams, M.L. Gala, K. Manthiram, Non-aqueous gas diffusion electrodes for rapid ammonia synthesis from nitrogen and water-splitting-derived hydrogen, Nat. Catal. 3 (2020) 463–469.
- [25] K. Li, S.Z. Andersen, M.J. Statt, K. Krempel, R. Sazinas, J.B. Pedersen, V. Shadravan, J.K. N  rskov, I. Chorkendorff, Enhancement of lithium-mediated ammonia synthesis by addition of oxygen, Science 374 (2021) 1593–1597.
- [26] H.K. Lee, C.S.L. Koh, Y.H. Lee, C. Liu, X. Han, C. Tsung, X.Y. Ling, Favoring the unfavored: selective electrochemical nitrogen fixation using a reticular chemistry approach, Sci. Adv. 4 (2018) eaar3208.
- [27] A. Medford, J. Wellendorff, A. Vojvodic, F. Studt, F.A. Pedersen, K.W. Jacobsen, T. Bligaard, J.K. N  rskov, Assessing the reliability of calculated catalytic ammonia synthesis rates, Science 345 (2014) 197–199.
- [28] K. Honkala, A. Hellman, I.N. Remediakis, A. Logadottir, A. Carlsson, S. Dahl, C. H. Christensen, J.K. N  rskov, Ammonia synthesis from first-principles calculations, Science 307 (2005) 555–558.
- [29] Q. Liu, T. Xu, Y. Luo, Q. Kong, T. Li, S. Lu, A.A. Alshehri, K.A. Alzahrani, X. Sun, Recent advances in strategies for highly selective electrocatalytic N₂ reduction toward ambient NH₃ synthesis, Curr. Opin. Electrochem. 29 (2021).
- [30] Y. Sun, W. Wu, L. Yu, S. Xu, Y. Zhang, L. Yu, B. Xia, S. Ding, M. Li, L. Jiang, J. Duan, J. Zhu, S. Chen, Asymmetric acidic/alkaline N₂ electrofixation accelerated by high-entropy metal-organic framework derivatives, Carbon Energy (2022) 1–12.
- [31] S.L. Foster, S.I.P. Bakovic, R.D. Duda, S. Maheshwari, R.D. Milton, S.D. Minteer, M. J. Janik, J.N. Renner, L.F. Greenlee, Catalysts for nitrogen reduction to ammonia, Nat. Catal. 1 (2018) 490–500.
- [32] Q. Li, P. Shen, Y. Tian, X. Li, K. Chu, Metal-free BN quantum dots/graphitic C₃N₄ heterostructure for nitrogen reduction reaction, J. Colloid Interface Sci. 606 (2022) 204–212.
- [33] P. Mehta, P. Barboun, F.A. Herrera, J. Kim, P. Rumbach, D.B. Go, J.C. Hicks, W. F. Schneider, Overcoming ammonia synthesis scaling relations with plasma-enabled catalysis, Nat. Catal. 1 (2018) 269–275.
- [34] Z.Y. Wu, M. Karamad, X. Yong, Q. Huang, D.A. Cullen, P. Zhu, C. Xia, Q. Xiao, M. Shakouri, F.Y. Chen, J.Y.T. Kim, Y. Xia, K. Heck, Y. Hu, M.S. Wong, Q. Li, I. Gates, S. Siahrostami, H. Wang, Electrochemical ammonia synthesis via nitrate reduction on Fe single atom catalyst, Nat. Commun. 12 (2021) 2870.
- [35] Z. Li, Z. Deng, L. Ouyang, X. Fan, L. Zhang, S. Sun, Q. Liu, A.A. Alshehri, Y. Luo, Q. Kong, X. Sun, CeO₂ nanoparticles with oxygen vacancies decorated N-doped carbon nanorods: a highly efficient catalyst for nitrate electroreduction to ammonia, Nano Res. 15 (2022) 8914–8921.
- [36] Y. Hao, Y. Guo, L. Chen, M. Shu, X. Wang, T. Bu, W. Gao, N. Zhang, X. Su, X. Feng, J. Zhou, B. Wang, C. Hu, A. Yin, R. Si, Y. Zhang, C. Yan, Promoting nitrogen electroreduction to ammonia with bismuth nanocrystals and potassium cations in water, Nat. Catal. 2 (2019) 448–456.
- [37] J. Choi, H. Du, M. Chatti, B.H.R. Suryanto, A.N. Simonov, D.R. MacFarlane, Reassessment of the catalytic activity of bismuth for aqueous nitrogen electroreduction, Nat. Catal. 5 (2022) 382–384.
- [38] Y. Yao, S. Zhu, H. Wang, H. Li, M. Shao, A. Spectroscopic, Study of electrochemical nitrogen and nitrate reduction on rhodium, Surf., Angew. Chem. Int. Ed. 59 (2020) 10479–10483.
- [39] D. Yao, C. Tang, L. Li, B. Xia, A. Vasileff, H. Jin, Y. Zhang, S.Z. Qiao, In Situ fragmented bismuth nanoparticles for electrocatalytic nitrogen reduction, Adv. Energy Mater. 10 (2020).
- [40] Y. Wang, M.M. Shi, D. Bao, F.L. Meng, Q. Zhang, Y.T. Zhou, K.H. Liu, Y. Zhang, J. Z. Wang, Z.W. Chen, D.P. Liu, Z. Jiang, M. Luo, L. Gu, Q.H. Zhang, X.Z. Cao, Y. Yao, M.H. Shao, Y. Zhang, X.B. Zhang, J.G. Chen, J.M. Yan, Q. Jiang, Generating defect-rich bismuth for enhancing the rate of nitrogen electroreduction to ammonia, Angew. Chem. Int. Ed. 58 (2019) 9464–9469.
- [41] S. Wang, X. Hai, X. Ding, K. Chang, Y. Xiang, X. Meng, Z. Yang, H. Chen, J. Ye, Light-switchable oxygen vacancies in ultrafine Bi₅O₇Br nanotubes for boosting solar-driven nitrogen fixation in pure water, Adv. Mater. 29 (2017), 1701774.
- [42] W.P. Utomo, M.K.H. Leung, Z. Yin, H. Wu, Y.H. Ng, Advancement of bismuth-based materials for electrocatalytic and photo(electro)catalytic ammonia synthesis, Adv. Funct. Mater. 32 (2021).
- [43] Z. Fang, P. Wu, Y. Qian, G. Yu, Gel-derived amorphous bismuth-nickel alloy promotes electrocatalytic nitrogen fixation via optimizing nitrogen adsorption and activation, Angew. Chem. Int. Ed. 60 (2021) 4275–4281.
- [44] Y. Yao, S. Zhu, H. Wang, H. Li, M. Shao, A. Spectroscopic, Study on the nitrogen electrochemical reduction reaction on gold and platinum surfaces, J. Am. Chem. Soc. 140 (2018) 1496–1501.
- [45] J. Ren, C. Wan, T. Pei, X. Lv, Z. Yuan, Promotion of electrocatalytic nitrogen reduction reaction on N-doped porous carbon with secondary heteroatoms, Appl. Catal. B 266 (2020).
- [46] W.J. Grigsby, D. Steward, R.A. Franich, Production of amino-functionalised condensed tannins via a single step conversion using supercritical fluid, Process., J. Wood Chem. Technol. 41 (2021) 65–71.
- [47] B. Ostoji  , P. Schwerdtfeger, P.R. Bunker, P. Jensen, An ab initio study of SbH₂ and BiH₂: the Renner effect, spin–orbit coupling, local mode vibrations and rovibronic energy level clustering in SbH₂, J. Mol. Spectrosc. 330 (2016) 130–141.
- [48] J. Kubota, K. Aika, Infrared studies of adsorbed dinitrogen on supported ruthenium catalysts for ammonia, J. Phys. Chem. 98 (1994) 11293–11300.